Takashi Tonegawa[1]*, Shunsuke Takemura[2], Suguru Yabe[3], Kiyoshi Yomogida[4]

[1] Japan Agency for Marine-Earth Science and Technology (JAMSTEC), 2-15, Natsushima, Yokosuka Kanagawa, 237-0061, Japan.

[2]Earthquake Research Institute, the University of Tokyo, 1-1-1, Yayoi, Bunkyo, 113-0032, Japan.

[3]National Institute of Advanced Industrial Science and Technology, 1-1-1, Umezono, Tsukuba, Ibaraki, 305-8560, Japan.

[4]Hokkaido University, Kita-10, Nishi-8, Kita-ku, Sapporo, 060-0810, Japan.

Corresponding author: Takashi Tonegawa (tonegawa@jamstec.go.jp)

Key Points:

- Transient changes of seismic heterogeneities occurred 0-9 months before slow earthquakes in the shallow Nankai subduction zone.
- We consider that the heterogeneity changes are caused by fluid migration.
- The difference in timings between fluid migration and slow earthquakes reflects the pore pressure levels at the source regions.

Abstract

Fluid migration in subduction zones is a key controlling factor of slow and megathrust earthquakes at plate boundaries. During the migration, seismic velocity and heterogeneous structures in its pathways may be temporarily varied, preferably triggering slow earthquakes. Here, we show that transient changes of seismic heterogeneity occurred 0-9 months before shallow slow earthquakes in the Nankai subduction zone, Japan, using very long-term (6–10 y) records of ambient seafloor noise. The heterogeneity changes preceding to shallow slow earthquakes were observed near the margin of the source region, while concurrent changes primarily occurred in the source region. We propose that the heterogeneity changes are attributed to dynamic fluid migration, and the difference in timings reflects the pore pressure level in the corresponding source region. When fluids are supplied to a source region under relatively low pressure, fluids are leaked out from its downdip or updip side, and slow earthquakes occur not immediately but with a time delay of at most 9 months. In the high pore pressure case, slow earthquakes occur immediately with fluid migration from the source region. This study suggests that the heterogeneous seismic structure is possibly changed by fluid migration before slow earthquakes in the Nankai subduction zone.

Plain Language Summary While the linkage between fluid and slow earthquakes occurring at the plate boundary of subduction zones has been revealed, such a relationship for very shallow parts close to trench axes remains elusive. In this study, we investigated the temporal variations of seismic velocity and heterogeneous structure beneath the seafloor in the Nankai subduction zone,

Japan, using the seismographs observed by a permanent cabled network starting in 2010. The intensities of seismic heterogeneous structures change 0–9 months prior to the shallow slow earthquakes, implying that the heterogeneous structure is altered by fluid migration that affects the slow earthquake generation. In the case of the fluid migration preceding to slow earthquakes, fluids are supplied to the source region with relatively low pore pressure levels, and the pore pressure level there increases until the timing of the slow earthquake generation. In contrast, the case of concurrent fluid migration corresponds to the fluids supplied to the source region with a relatively high pore pressure level, and slow earthquakes occur at the immediate timing of the fluid supply. These results suggest that monitoring heterogeneous seismic structures potentially contributes to further understanding of the spatio-temporal relationship between fluid migration and shallow slow earthquakes.

1 Introduction

Slow earthquakes at plate boundaries have been observed in various subduction zones (Obara & Kato, 2016). They occur at both shallower and deeper extensions of megathrust seismogenic zones, and affect stress conditions in the vicinity of the megathrust zones. Their slow ruptures are likely related to the fluid near plate boundaries, and seismic evidence of the relationship between deep slow earthquakes and such fluids has been documented (Kodaira et al. 2004; Shelly et al. 2007; Katayama et al. 2012; Audet & Bürgmann 2014; Nakajima & Hasegawa 2016). Some studies have further suggested a temporal relationship between fluid migration and slow earthquakes.

For example, a study on the Hikurangi subduction zone suggested that the upward fluid migration from fault zones within the underlying oceanic crust occurs at the downdip end of slow slip events (SSEs) that expand to the trench, which activated slow earthquakes at the plate boundary (Warren-Smith et al. 2019). A receiver function study in the deep Cascadia subduction zone found changes in seismic velocity within a low-velocity layer at the top of the subducting plate after episodic tremor and SSEs, and suggested that the changes responded to fluctuations of pore-fluid pressure within the layer (Gosselin et al. 2020). Although a previous paper (Zal et al. 2020) shows, through the estimations of seismic anisotropy and velocity, that such a fluid migration may occur in shallow subduction zones, there have been few evidences on the linkage between dynamic structural variations associated with fluid migration and the preparatory-to-generation stages of slow earthquakes. Consequently, fluid-migration characteristics have been poorly understood, such as time scales and pathway repeatability, and their relationship to shallow slow earthquakes. Revealing these characteristics significantly contribute to the understanding of how fluids in the crust are related to the generation of shallow slow earthquakes, as well as the dynamic fluid processes occurring in subduction zones.

Because fluid migration may temporarily change seismic velocity and heterogeneity, here we shall investigate temporal variations in the seismic structure of the Nankai accretionary prism, Japan, by ambient noise analyses, using very

long-term seismic records (6–10 years) continuously observed at the seafloor. Ambient noise correlations of two receivers are capable of retrieving the background wavefield propagating between them (Shapiro et al. 2005; Brenguier et al. 2007). In the subsequent sections, we explain the application of the ambient noise correlation to extract temporal variations of seismic velocity and heterogeneous structure, and the location estimation of the heterogeneous structure changes. Moreover, we propose a possible mechanism to support our findings on the temporal variation of seismic structure.

2 Data

The ambient noise correlation was applied to continuous records in the vertical component of 49 stations in the Dense Oceanfloor Network system for Earthquakes and Tsunamis (DONET) deployed off the Kii Peninsula (Fig. 1) (Kaneda et al. 2015; Kawaguchi et al. 2015; Aoi et al. 2020). DONET1 and DONET2 of DONET are the eastern and western cabled networks deployed at water depths of 1,000-4,400 m since the end of 2010 and 2014, respectively. We examined the records observed by 20 stations in the period between 2011 and 9 March 2021 in DONET1 and 29 stations in the period between 2015 and 9 March 2021 in DONET2.

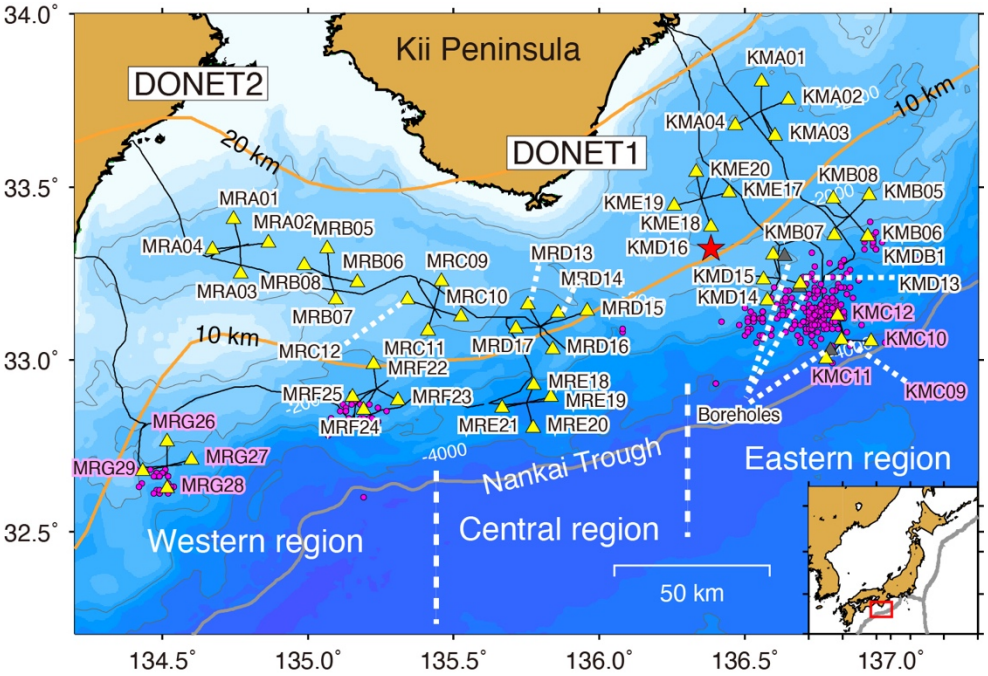

Figure 1. Map showing locations of stations and seismic velocity changes (*dv/v*). Yellow triangles and magenta circles represent DONET stations and shallow very low frequency earthquakes (sVLFE) during August 2015–April 2016 (Nakano et al. 2016; 2018).

The red star shows the location of the earthquake that occurred southeast of the Kii Peninsula on 1 April 2016. Grey triangles indicate the locations of the boreholes used in Araki et al. (2019) and Ariyoshi et al. (2021). Nodes KMC and MRG (pink) are used in Fig. 3. Orange lines represent the depth contour of the Philippine Sea Plate (Baba et al. 2002; Hirose et al. 2008).

3 Methods

3.1 Calculation of cross-correlation functions

We used ambient noise records at frequencies of 0.5–2.0 Hz. When tremors were active in the accretionary prism toe, tremor signals at frequencies lower than 2 Hz were observed although the dominant frequencies of their signals were 2–8 Hz. Rayleigh waves from large teleseismic and regional earthquakes were also observed in this frequency band. To suppress such energetic signals, we used a method introduced by Tonegawa et al. (2021), and prepared the following log-normal-shaped function.

$F(t) = \frac{1}{\sqrt{2\pi\sigma(t/T)}} exp\left\{-\frac{(\log(\frac{t}{T}))^2}{2\sigma^2}\right\}$ (1),

where = 2 and T = 400 s. The cosine taper with a time window of 20 s was also applied to both the edges of the function. The root-mean-squared ($\mathrm{RMS_{1hour}}$) amplitudes were calculated with one-hour continuous records. If amplitudes in the one-hour record, A_{max}, exceeded five times of the $\mathrm{RMS_{1hour}}$, the original records were divided by the following function with a time shift of 80 s from the time of A_{max},

$S(t) = C \bullet F(t)$ (2),

where

$C = 3A_{\mathrm{max}}/\mathrm{RMS_{1hour}}$ (3).

The maximum amplitude of the log-normal shaped function (Eq. (1)) was approximately 80 s from the starting time. The examples are shown in Fig. S1.

The CCFs were calculated using a time window of 400 s with spectral whitening (Brenguier et al. 2007) and were stacked over 30 days. When the RMS of one segment (400 s) in the processed (partially suppressed) records was less than 0.4 times of the RMS of the time series of 3600 s, we discarded the segment (Fig. S1). In the subsequent processing, we only used waveforms stacked over >75 % of CCFs for 30 days. The resulting cross-correlation functions (CCFs) at frequencies of 0.5–2.0 Hz revealed ocean acoustic-coupled Rayleigh (ACR) waves propagating in the ocean and the entire accretionary prism (Tonegawa et al. 2015). Since the obtained CCFs were stable over the entire observation period (Fig. 2a), we estimated temporal variations in the seismic velocity and the heterogeneous structure within the accretionary prism in comparison with slow earthquake activities.

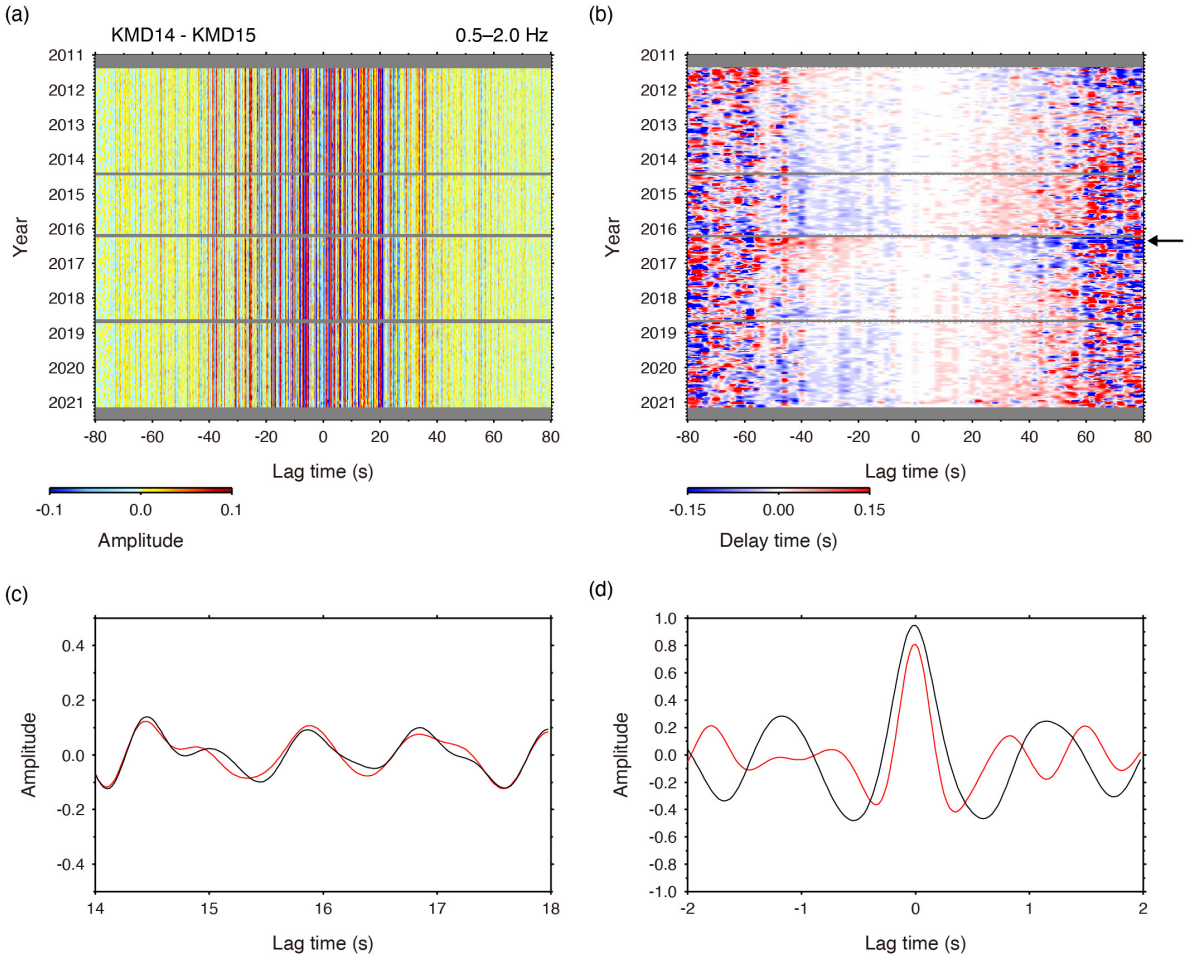

Figure 2. Example of the processing of stretching. (a) CCFs for the KMD14–KMD15 station pair over the observation period at 0.5–2.0 Hz. (b) Delay times of CCFs in (a) with respect to the reference CCF stacked over the first 1 year. The arrow indicates the timing of the off-Mie earthquake. (c) Parts of (black line) the CCF (203 Julian day in 2013) and (red line) reference CCF at a lag time of 14–18 s. (d) (black line) Cross-correlation function and (red line) Wiener filter between the two CCFs shown in (c).

3.2 Measurement of velocity and waveform changes

We examined the stretching method to measure seismic velocity changes (Sens-Schonfelder & Wegler 2006). However, prior to this, we confirmed whether the coda part of the obtained 30-day CCFs is indeed stretched and contracted during the observation period by applying the Wiener filter (Wiener 1949). The reference CCFs were prepared by stacking CCFs over the first year from the

starting time of the observation of station pairs. Using a time window of 4 s between 2 s and 82 s and a time step of 2 s, we calculated the Wiener filter that transforms the reference CCF into the individual 30-day CCF, in which the lag time of an impulsive peak in the Wiener filter is the differential time of the segments between the reference and individual CCFs. The Wiener filter was calculated in the frequency domain, and it showed an impulsive peak that allowed for accurate measurements of the time differences, compared to the use of cross correlation function (Figs. 2c and d). An example in Fig. 2b shows that the time difference between the reference and individual CCFs becomes large as the lag time increases, and also a sudden trend change due to a nearby earthquake (M_w 5.9) occurred southeast of the Kii Peninsula on 1 April 2016 (Fig. 1). Moreover, no seasonality was observed in our measurements, which indicates that the obtained results are primarily based on the stable background wavefield from the azimuthal range of NE to SE in all seasons (see more details for Text S1).

The time window of 50 s, from the theoretical arrival time of the ACR wave in the reference CCF, was stretched to match that of the individual CCF in which the theoretical time was calculated with a separation distance of two stations and a propagation velocity of 1.5 km/s. The searching range of the stretch (dt/t) was −0.4–0.4 %, and $dv/v = -dt/t$. We also calculated the cross-correlation coefficients (CCs) of the 50-s segments between the reference CCF and the individual CCFs that were stretched using the obtained dv/v (Obermann et al. 2013). We plotted the obtained dv/v (Fig. 3 and Figs. S2 and S3) and CC (Fig. 3 and Figs. S4–S6) as a function of time. The dv/v and CC represent the seismic velocity and heterogeneity changes around a pair of two stations. The 1 uncertainties of dv/v and CC were estimated by averaging those values over ±50 days. The obtained dv/v (Figs. 3a and Fig. S2) in the period near the earthquake was consistent with that in a previous study (Ikeda and Tsuji 2018).

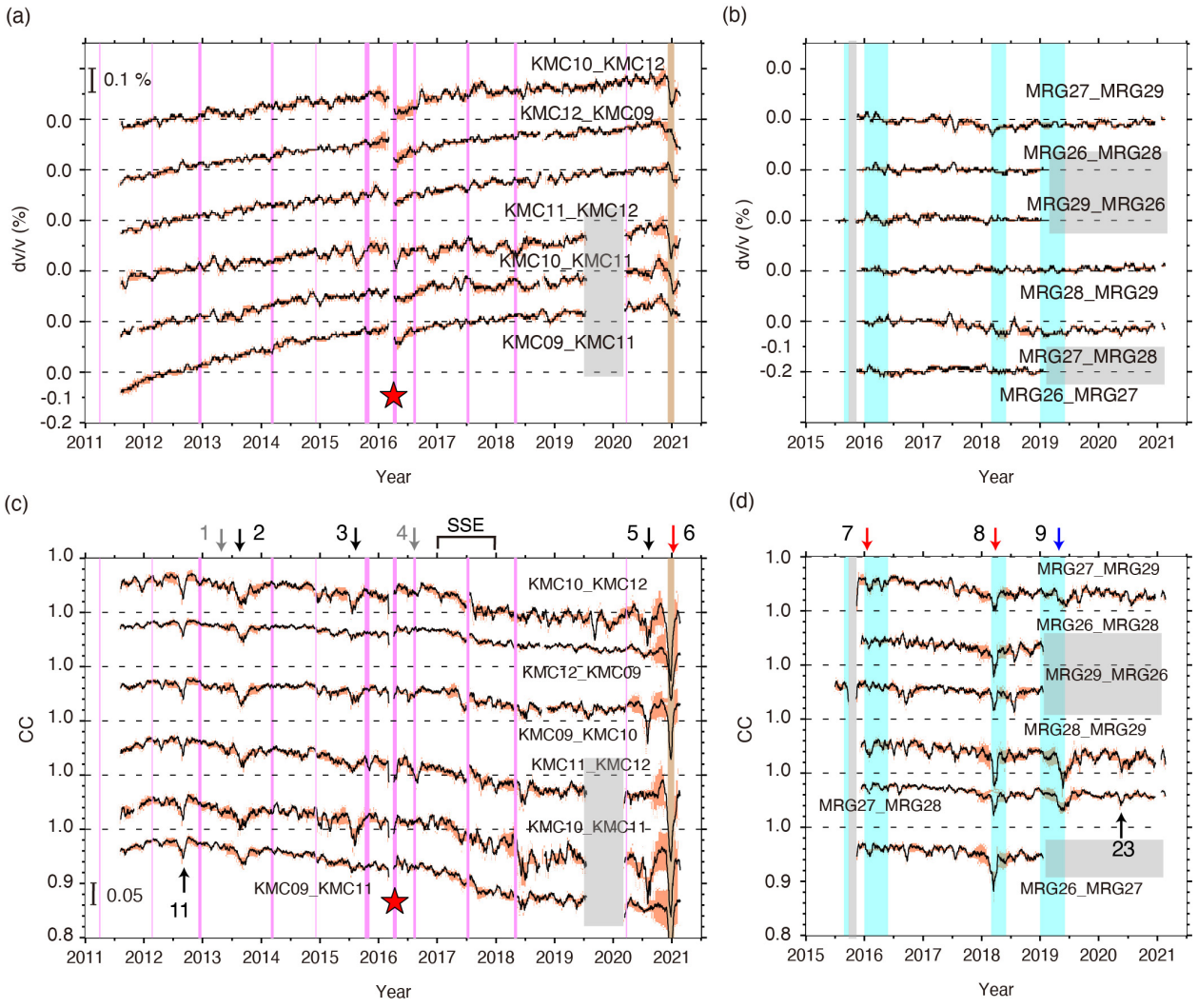

Fig. 3. Temporal changes of seismic velocity and heterogeneity. (a) The resulting *dv/v* for 6 pairs of 4 stations of node KMC with (orange) 1 uncertainties for ±50 days. Pink, light-brown, and gray regions represent the periods of SSEs from Araki et al. (2017) and Ariyoshi et al. (2021), a large slow earthquake activity, and data gaps. Red star shows the earthquake in Fig. 1. (b) Same as (a), but for node MRG. Light-blue regions indicate the periods of sVLFE activities (Nakano et al. 2016; 2018; Takemura et al. 2019; Baba et al. 2020). (c) Temporal CC variation for node KMC. Black and gray arrows indicate the preceding CC reductions observed around node KMC and other regions in the southern part of DONET, respectively. Red arrow shows concurrent CC reductions. Other numbers are

provided in Fig. 4. An SSE was detected by the seafloor geodetic observation in 2017 (Yokota and Ishikawa 2020). (d) Same as (c), but for node MRG. Blue arrow represents concurrent CC reductions with a slight delay.

The reliabilities of the obtained *dv/v* and CC were confirmed by examining the stacking periods of 20 and 60 days, instead of 30 days (Fig. S7). The *dv/v* variations among the stacking periods of CCFs (20, 30, and 60 days) were negligible. By contrast, the averaged values of the obtained CC were large for the 60-day CCFs because the stacked CCFs became close to the reference CCF, and those for the 30-day and 20-day CCFs are comparable. Although the absolute values of CC were different among the stacking periods of CCFs, several CC reductions can be observed, and their timings observed in the 30-day CCFs could be clearly reproduced. We confirmed the reliabilities of *dv/v* and CC in terms of the count percentage of CCFs used in the 30-day CCFs for pairs of KMD13-KMD15 and KMC12-KMC09. Although several reductions of the count percentages of the CCFs were observed, they did not match with CC reductions, indicating that the obtained CC reductions did not reflect the lack of CCFs for stacking. Moreover, we confirmed that the obtained CC reductions do not correlate with the ocean environment (parameters) around this region (See details for Text S2).

To further investigate spatial variations of CC reductions in the southern part of DONET1, we calculated CCFs for all station pairs at nodes KMB, KMC, and KMD, and aligned CC measurements using the CCFs as a function of central location of two stations (Figs. 4 and S4e), in which CC values in 4 adjacent traces are averaged to enhance their coherencies. To remove long-term trends, we calculated 100-day moving averages of the original CC variations with 5 times, and subtracted them from the original CC variations (Fig. S4e). Also, we discarded pairs with a separation distance of >30 km between two stations because CC perturbations in such cases are relatively large and hence unstable. To specify CC reductions, we plotted the CC variations smaller than 2 times of the standard deviation for each trace (Figs. 4c and d). Here, the standard deviation was calculated using CC variations over the entire observation period for each pair of stations. It is considered that the CC reductions reflect the temporal changes in the heterogeneous seismic structure, and those changes are caused by fluid migration at a local scale. The relationship between CC reductions and slow earthquakes is summarized in Table S1.

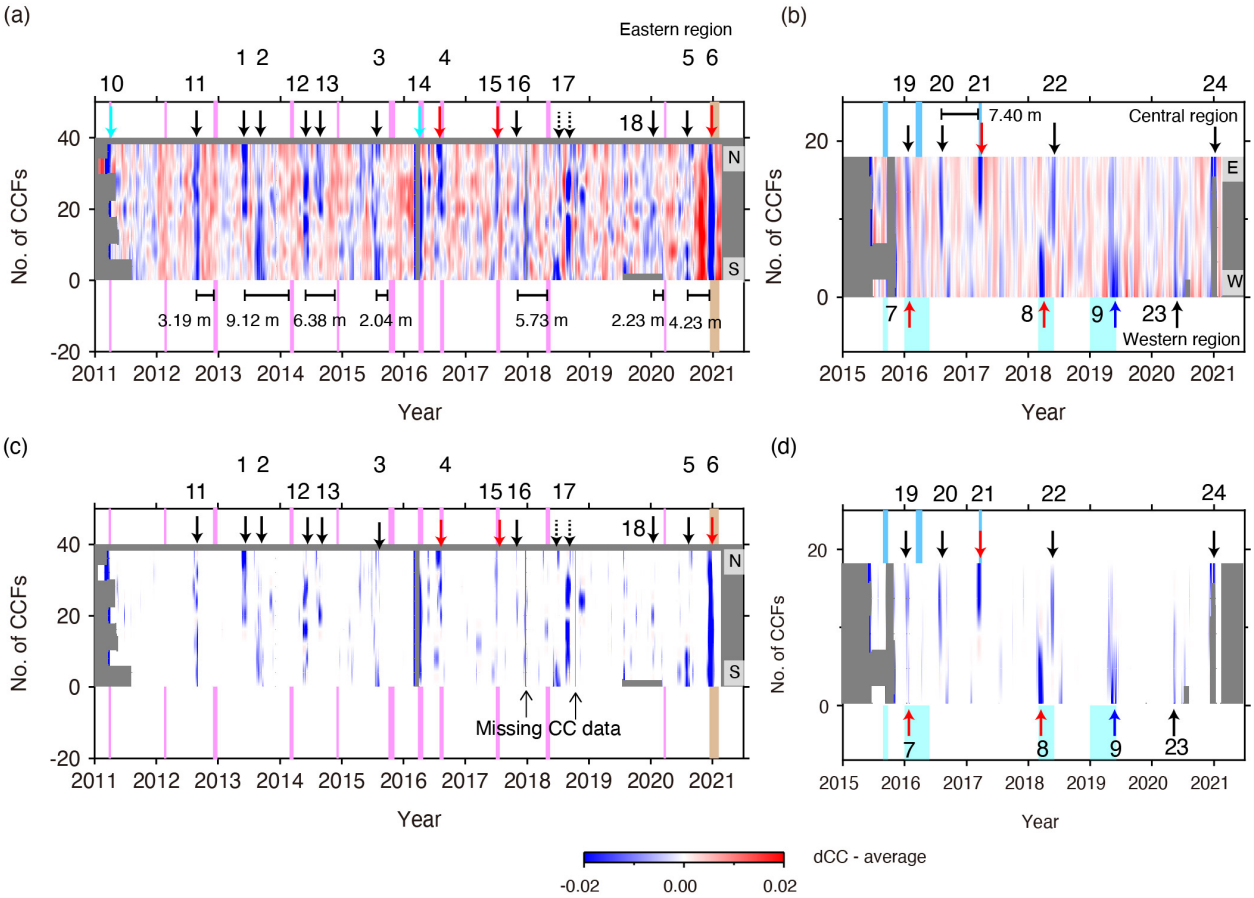

Fig. 4. Identification of CC reductions. (a) CC variations for station pairs in the southern part of DONET1 (nodes KMB, KMC, and KMD), which are aligned by the central locations of station pairs from south (bottom) to north (top). Black and red arrows indicate pairs that show preceding and concurrent CC variations to slow earthquakes, respectively. Blue arrow corresponds to concurrent CC reductions but with a delay (Event 9). Light-blue arrow corresponds to CC variations associated with large earthquakes (Event 1 of the 2011 Tohoku-Oki earthquake, and Event 14 of the earthquake shown in Fig. 1). More details for each event are described in the text and Table S1. Pink (Araki et al. 2017; Ariyoshi et al. 2021) and light-brown regions are the periods of slow earthquakes. Periods from first CC drop and subsequent slow earthquake activities are noted. (b) Same as (a), but for the southern part of DONET2 (MRE, MRF, and MRG), which are aligned by the central locations of station pairs from west (bottom) to east (top). Dark-blue and light-blue represent sVLFE activities around MRE (central region)

and MRF–MRG (western region), respectively (Nakano et al. 2016; 2018; Takemura et al. 2019; Baba et al. 2020). (c) Same as (a), but the CC reductions that are larger than twice the standard deviation are only plotted. (d) Same as (c), but for DONET2.

3.3 Seismic scattering coefficient

To estimate the region where the heterogeneous seismic structure was changed, we mapped scattering coefficient changes (SCCs) by a method referred to previous studies (Obermann et al. 2013; Sánchez-Pastor et al. 2018; Hirose et al. 2019; Hirose et al. 2020). We adopted the dataset of *dCCi* defined as the CC difference between the value averaged ±5 days around the reduced bottom and the value averaged between 60 and 90 days prior to the reduced CC for the *i*-th pair of two stations. The observed dCC_i can be expressed as

$$\mathrm{dCC} = \mathrm{Gm} \quad (4)$$

where **dCC** is the vector of dCC_i (i=1…n). **G** is the matrix with

$$G_{\mathrm{ij}} = \frac{s}{t} K_{\mathrm{ij}} \quad (5),$$

where Δs is the area of the cell, t is the centre of the time interval in the coda part where the stretching is evaluated, and **m** consists of the SCCs for each cell j to be estimated. K_{ij} is the sensitivity kernel for station pair i in cell j, and K in $\mathbf{x_0}$ can be described by the positions of two stations, $\mathbf{s_1}$ and $\mathbf{s_2}$, as

$$K\left(\mathbf{s_1}, \mathbf{s_2}, \mathbf{x_0}, t\right) = \frac{\int_0^t p(\mathbf{s_1}, \mathbf{x_0}, u) p(\mathbf{x_0}, \mathbf{s_2}, t-u) \mathrm{du}}{p(\mathbf{s_1}, \mathbf{s_2}, t)} \quad (6).$$

$p(\mathbf{s_1}, \mathbf{s_2}, \mathrm{t})$ is the probability that the waves have propagated from $\mathbf{s_1}$ to $\mathbf{s_2}$ in time t, and this can be approximated by the intensity of the wavefield from $\mathbf{s_1}$ to $\mathbf{s_2}$ at time t. The analytic two-dimensional solution of the radiative transfer for isotropic scattering for the intensity propagator is given by

$$p(r,t) = \frac{e^{-\frac{ct}{l}}}{2\pi r}\delta(ct-r) + \frac{1}{2\pi l ct}\left(1-\frac{r^2}{c^2t^2}\right)^{-\frac{1}{2}} \exp^{\left[\sqrt{c^2t^2-r^2}-ct\right]/l} \Theta(ct-r) \quad (7),$$

where c is the group velocity of the wave, r is the distance between source and receiver, l is the transport mean free path, and $\Theta(x)$ is the Heaviside step function. An example of the sensitivity kernel is shown in Fig. 8a. The theoretical dCC_i in $\mathbf{x_0}$ can be computed by

$$\mathrm{dCC}_i^{\mathrm{th}}\left(\mathbf{s_1}, \mathbf{s_2}, \mathbf{x_0}, t\right) = \frac{c\, g}{2} K\left(\mathbf{s_1}, \mathbf{s_2}, \mathbf{x_0}, t\right) \quad (8),$$

where Δg is an amount of the SCC over the area covering $\mathbf{x_0}$ related to the strength and size of the change in the heterogeneous seismic structure.

In this study, we used $c = 1.5$ km/s for the ACR wave. We also estimated the transport mean free path l following the method of previous studies (Hirose et al. 2019; Hirose et al. 2020). The envelope amplitudes of the observed CCFs of station pairs are fitted with eq. (7) multiplied by e^{-bt} by a grid search in the domain of the transport mean free path l and the intrinsic absorption b. We searched the minimum value for the following equation,

$SSR = \sum_{k=1}^{6} \sum_{m=1}^{M} \left(p_{\mathrm{obs}}\left(t_k, m\right) exp(-bt_k) - p_{\mathrm{syn}}(t_k, j) exp(-bt_k) \right)^2$ (9),

where k is the number of time windows in the coda, and m is the number of station pairs. The envelope functions were normalized by the envelope amplitude at a lag time of 80 s. The time windows of 20–24 s, 24–28 s, 28–32 s, 32–36 s, 36–40 s, and 40–44 s were selected, and the normalized amplitudes of the first and second terms were averaged over the time windows. Transport mean free path and intrinsic absorption were estimated at 10.8 km and 0.006 s^{-1} using grid search at 0.5–2.0 Hz, respectively (Fig. 8b), and 14.0 km and 0.010 s^{-1} at 0.2–0.5 Hz whose values were used in the section 3.5.

3.4 Non-linear inversion by simulated annealing

We used simulated annealing, a kind of non-linear inversion, to stably find the global minimum of the optimisation problem (Sen & Stoffa, 1995). Simulated annealing adopts a Monte Carlo method and searches the global minimum by slowly lowering the possibility of the acceptance of random perturbations to model parameters with decreasing temperature. The methodology of the Δg update was based on a previous study on the simulated annealing (Chevrot 2002). An optimal estimate of Δg is obtained by minimising the cost function:

$E = \sum_{i=1}^{n} \left| \mathrm{dCC}_i - \mathrm{dCC}_i^{\mathrm{th}} \right|$ (10).

This value is iteratively estimated (E_k: $k = 0 \ldots m$) through random perturbations of Δg_j in each cell j. The perturbation is fully accepted with ΔE_k ($= E_{k+1} - E_k$; $k = 0 \ldots m$) 0, while, with $\Delta E_k > 0$, the perturbation is accepted with the probability

$P = e^{-\frac{\Delta \mathrm{E}_k}{T_k}}$ (11),

where T_k is temperature. The annealing schedule at the k-th iteration is given by $T_k = {}^{\mathrm{k}}T_0$, with the initial temperature of $T_0 = 3E_0$ and the cooling rate of = 0.996. The perturbation is accepted in the case of P_j by selecting a random number between 0 and 1 at each iteration.

At each iteration, $\Delta g_{\ j}$ in cell j is perturbed by the selected random number as,

$$g_j^{'} = \begin{cases} g_j - A & if\ \alpha < 0.5 \\ g_j + A & if\ \alpha > 0.5 \end{cases}, \quad (12)$$

where the perturbation of A is 0.0001. Because Δg is necessarily positive in this study, the update was not performed at the cells when $g_j^{'} < 0$. The time t in eqs. (3–4) and the cell size were set at 35 s and 5 km × 5 km over (32.8°N, 136.4°E) × (33.65°N, 137.1°E) in space, respectively. The uncertainty in the present non-linear inversion was estimated by changing seeds of random numbers for 10 times, and their standard deviations were estimated. The result of the SCCs and their errors are shown in Figs. 6, S10 and S11. Because the separation distance of the nodes in DONET2 is larger than that in DONET1, we did not estimate the spatial distribution of SCCs in DONET2.

3.5 Verification from numerical simulation

We verified the aforementioned method using synthetic waveforms calculated by the Open source Seismic Wave Propagation Code software 'OpenSWPC' (Maeda et al. 2017) with three-dimensional velocity models. The simulation model covered an area of 110 × 110 × 65 km^3 with a uniform grid interval of 0.05 km. The stations of DONET1 and additional virtual stations were set, and the sources were randomly located within the donut-shaped ring at the sea surface (Fig. S11a). The triangle-shaped source time functions with a duration of 1 s were applied as a vertical force to the source locations with random lapse times between 0 and 500 s. This processing allows us to obtain a quasi-random wavefield at the synthetic stations. The time length of the simulated waveform was 500 s by calculating 200,000 time steps, but we calculated 5 times with randomly changing source locations and origin times of excitations under the above conditions. We used a time window of 100–400 s of the synthetic ambient noise records for calculating CCFs, and stacked the 5 CCFs at a frequency band of 0.2–0.5 Hz.

The stacked CCFs were estimated for three velocity models for (1) the original velocity model (Takemura et al. 2020), (2) the original velocity model with a velocity reduction of 0.2 % at the top of 1 km from the seafloor in the region shown in Fig. S11a, and (3) same as the model (2) but with a velocity reduction of 0.2 % within the entire accretionary prism. The stacked CCFs show clear ACR waves with a propagation velocity of 1.5 km/s (Fig. S11b). To measure *dCC*, we only used the CCFs for station pairs with separation distances less than 30 km in the nodes KMB, KMC, and KMD. We applied the stretching method (Sens-Schonfelder & Wegler 2006), measured the *dCC* between the CCFs of the models (1) and (2), and the *dCC* between the CCFs of the models (1) and (3) (Obermann et al. 2013), and then applied the simulated annealing inversion explained in the previous section to the synthetic *dCC* dataset. Here, we employed a transport mean free path of 14.0 km in the inversion. Consequently, the synthetic tests show that the SCCs in both cases were precisely estimated to the region where the velocity reductions were assigned (Figs. S11c and d). Therefore, this technique can precisely estimate the horizontal SCC locations, although the depth at which fluid migration occurs is difficult to specify.

4 Results

4.1 Temporal variation of seismic velocity

Measuring the degree of CCF stretching in the time domain, we estimated the seismic velocity changes ($dv/v = -dt/t$), assuming that the travel times of direct and multiply scattered waves in the CCFs were affected by the average velocity change between a pair of stations in the accretionary prism with a thickness of ~6 km. The resulting dv/v in the accretionary prism toe (nodes KMB, KMC, and KMD) showed gradual velocity increases of 0.1–0.2 % from 2011 to March 2016 (Fig. 3a), probably reflecting fluid drainage from the subseafloor parts into the seawater due to the sediment compaction primarily in a shallow part

of the accretionary prism (Fig. 5a). The occurrence of a nearby earthquake (M_w 5.9), southeast off the Kii Peninsula on 1 April 2016 (Fig. 1), suddenly reduced the seismic velocity, but the dv/v gradually increased again after the earthquake (Fig. 3a and Fig. S2). Such long-term gradual increase in dv/v over the observation periods was not observed in the landward region (nodes KMA and KME) or in the western part of the Nankai subduction zone (DONET2) (Fig. S3). The above remarkable changes in dv/v corresponded to the gradual increases caused by sediment compaction and the rapid reduction due to the local earthquake. Moreover, dv/v responded to a slow earthquake activity during December 2020–January 2021, which was the longest one during the DONET observation period, and this will be discussed later.

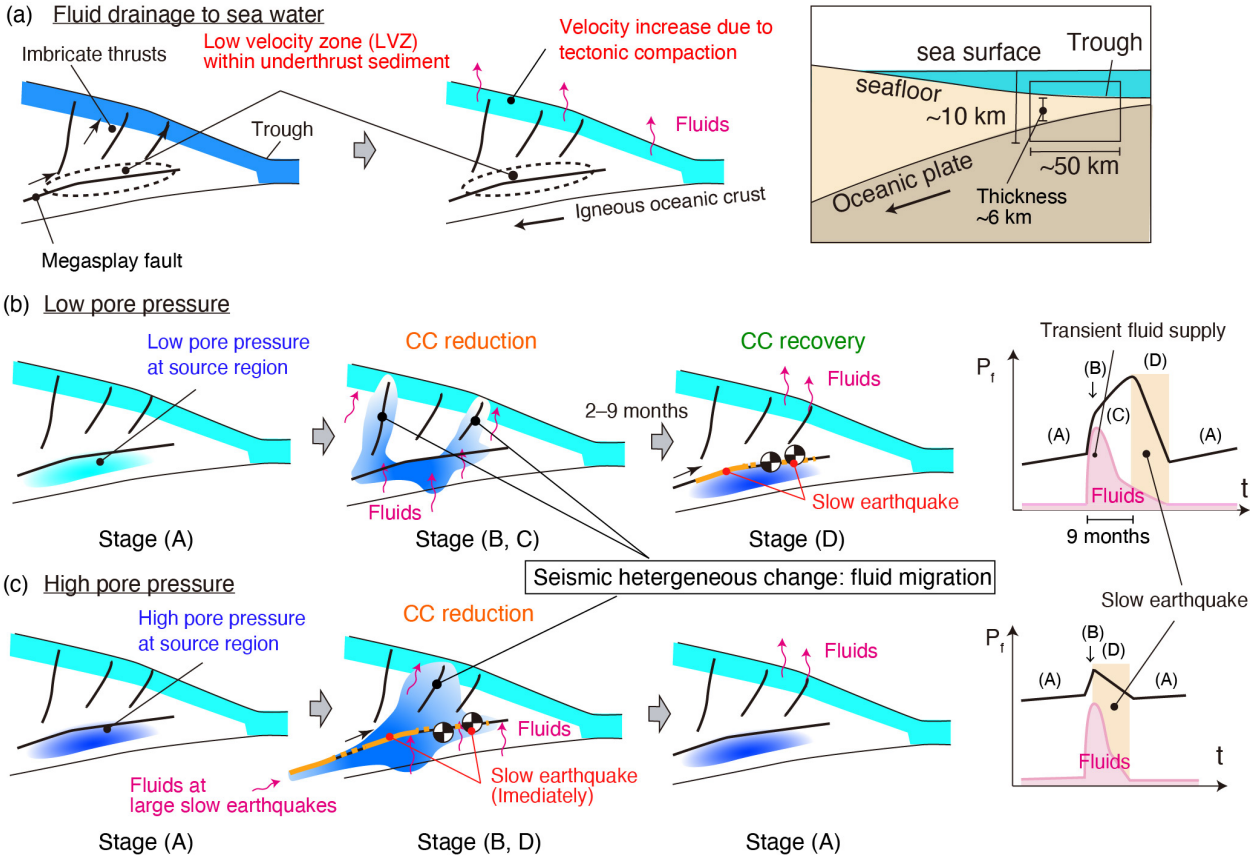

Fig. 5. Spatiotemporal relationship between fluid supply, slow earthquakes, and pore pressure. (a) Velocity increase at shallow depths due to fluid drainage to seawater, with a geological interpretation of Akuhara et al. (2020). Blue shades represent the amount of fluid. (b) Slow earthquake generation and fluid supply in the source region for low pore pressure. Beach balls and orange lines show

sVLFEs and SSEs. Magenta arrows indicate fluid flow. (Right) Temporal variation in pore pressure (P_f) at the source region for low pore pressure. Pink and light-orange areas indicate the amount of fluid supply to the source region and the activity period of slow earthquakes, respectively. The characters of A–D represent stages of P_f variations (see details in the text). (c–d) Same as (b), but for high pore pressure.

4.2 Temporal variation of seismic heterogeneity

Because waveforms in the CCFs respond to temporal changes in seismic heterogeneity due to fluid migration, temporal changes of the CCF waveform have been used to investigate temporal heterogeneity variations in a volcano (Obermann et al. 2013) and the focal region of an earthquake (Ikeda & Takagi 2019), and it was capable of detecting slight and local structural changes compared with that from *dv/v* variations.

Our results show that distinctive CC drops occurred both prior to (e.g., Events 1–3 and 5 in Fig. 3c; hereafter preceding CC reductions) and at the timing of (e.g., Events 4 and 6 in Fig. 3c and Events 7–9 in Fig. 3d; hereafter concurrent CC reductions) the short-term (<1 month) slow earthquakes in the southern part of the accretionary prism. Here, we referred to the SSEs derived from pore pressure variations observed at boreholes in DONET1 (Fig. 1) (Araki et al. 2017; Ariyoshi et al. 2021), and also the activities of shallow very low frequency earthquakes (sVLFEs) in DONET2 (Nakano et al. 2016; 2018; Takemura et al. 2019; Baba et al. 2020) because borehole sensors were not constructed in this region. Hereafter, we define these SSEs and sVLFEs as slow earthquakes. Preceding CC reductions are mainly observed in the eastern and central regions, and concurrent CC reductions are observed in the western region (see the region definition in Fig. 1). In the eastern and central regions, the occurrences of the preceding and concurrent CC reductions change depending on the time (Fig. 4). A comparison of other CC reductions with slow earthquakes is shown in Fig. 4 and discussed in the section 5.3. These CC drops were probably due to temporal changes in seismic heterogeneities with small amounts of fluid supply that did not significantly change *dv/v*. Such multiple preceding CC reductions roughly started 2–9 months prior to the slow earthquakes (the maximum preceding time was 9.12 months, Fig. 4) and continued for ~9 months thereafter (Fig. 3c). Moreover, two CC drops were sometimes observed during one inter slow earthquake period (e.g., Events 1 and 2, and Events 12 and 13 in Fig. 4).

Using the spatial distribution of CC reductions observed for each event, we estimated the spatial variation of SCC for the ACR waves. The results show that the locations of preceding and concurrent SCCs were estimated to be close to the margin of (Figs. 6a, b, c, and e) and inside (Figs. 6d and f) the source regions of shallow slow earthquakes, respectively. In particular, the SCC regions of the two CC reductions prior to a single SSE (Events 1 and 2 in Fig. 4) were located at the downdip and updip sides of the source region, respectively (Figs. 6a and b).

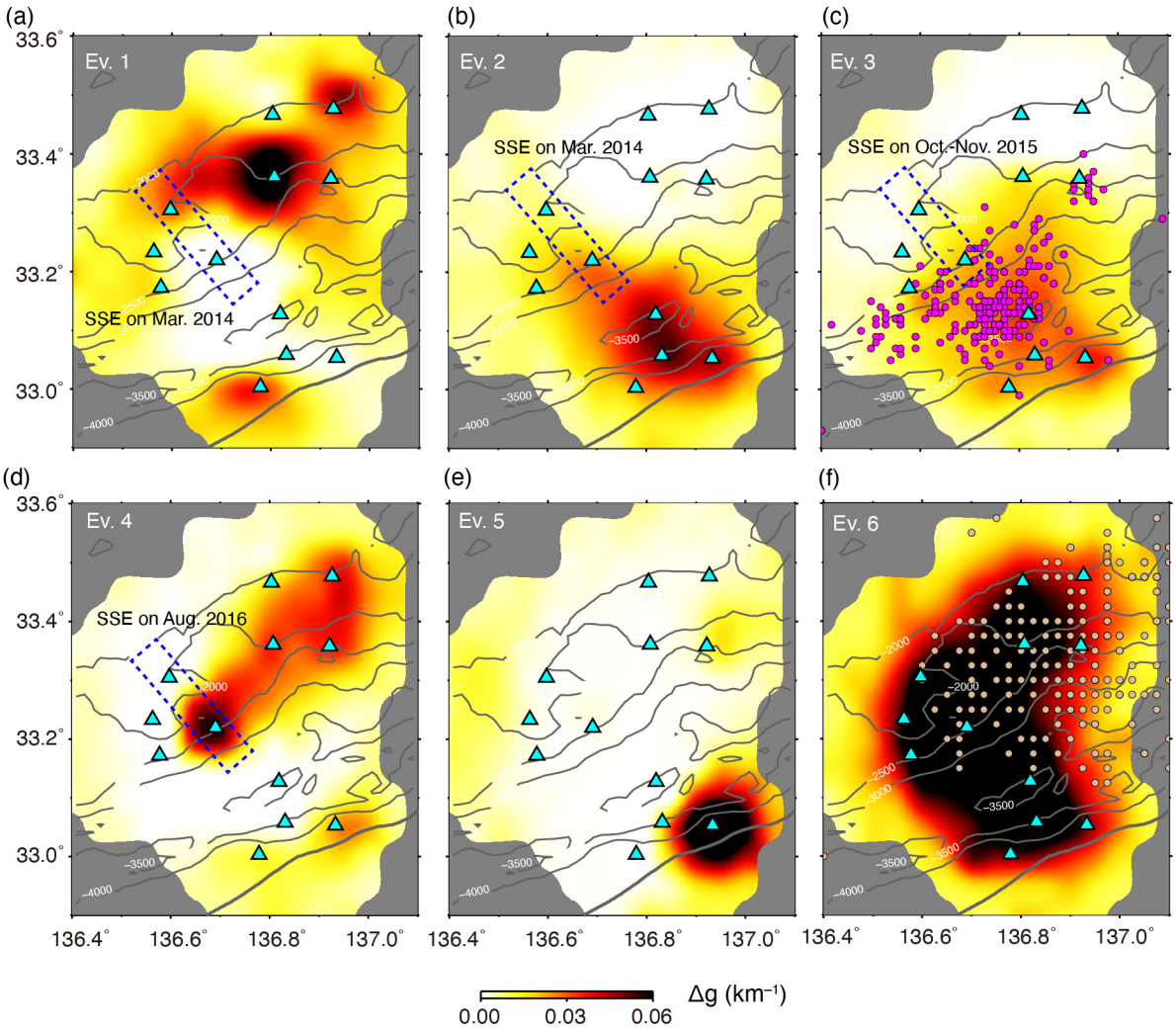

Fig. 6. Spatiotemporal variations of scattering coefficient changes (Δg). (a) Map showing the scattering coefficient changes in the southern part of DONET1 for Event 1 (the event numbers are shown in Fig. 4). Dashed blue-boxes represent the regions of SSEs detected by Araki et al. (2017) (the slip region only in the dip direction was referred from the paper). Light-blue triangles show the locations of the DONET stations for nodes KMB, KMC and KMD. (b–f) Same as (a), but for Events 2–6. Purple and light-brown circles in (c) and (f) show sVLFE locations during 2015 (Nakano et al. 2016; 2018) and December 2020–January 2021 (Takemura et al. 2021).

5 Discussion

5.1 dv/v variations and tectonic compression

Our results show that gradual velocity increases of 0.1–0.2 % within the accretionary prism toe in the eastern region, and such variations could be not be observed in the landward region of DONET1 and the entire region of DONET2. The gradual velocity increases are caused by fluid drainage from the subseafloor structure into the seawater. Because fluids are already expelled beneath the landward stations of DONET by tectonic compression (Kameda et al. 2011; Saffer & Tobin 2011), our observations that show no remarkable gradual changes in dv/v in the landward regions are plausible. However, the behaviour of dv/v in the accretionary prism toe in DONET2 remains elusive. It is considered that, compared to the eastern region, (1) the tectonic compression within the accretionary prism is weaker, (2) pathways of fluids to the seafloor within the prism are lesser, and (3) fluids within the prism supplied by the incoming plate are lesser. Seismic exploration survey results with high resolutions are required in these regions for investigating further details.

5.2 Spatial variation of pore pressure at the prism bottom

The underthrust sediment in the prism is characterized by low velocity (Park et al. 2010; Akuhara et al. 2020), high pore pressure (Tsuji et al. 2014), and a thickness of < 2 km, wherein the fluid concentration reduces the effective strength of the fault and induces slow earthquakes (Kitajima & Saffer 2012) (Fig. 5a). Although the seismic structure in the central and western regions (i.e., DONET2) has not been estimated densely, such low velocity zones are present in the accretionary prism toe (Tonegawa et al. 2017). Fluids are replenished to source regions of shallow slow earthquakes by compaction-driven dewatering from the underthrust sediments and dehydrations of the subducted hydrous minerals in the sediments and underlying oceanic crust (Saffer et al. 2008; Kameda et al. 2011; Saffer & Tobin 2011) (Figs. 5b and c). Moreover, there may be an additional mechanism for fluid supply. A slow earthquake activity occurred in the southern part of DONET1 from 6 December 2020 to 14 January 2021 (Fig. 4f), and its preceding CC reductions correspond to Event 5. Because the dv/v responded only to this slow-earthquake event (Fig. 2a) and the spatial variation of SCCs was extended over the southern part of DONET1 (Fig. 4f), a large quantity of fluids plausibly migrated during this event, inducing the highly-active slow earthquakes in the region where the SCC was observed. These observations may indicate that fluids were supplied not only from the nearby source region but also along the plate interface through transmegathrust fluid migration (Sibson 1992; Sibson 2013) (Fig. 5). In this scenario, the SSEs that extend to a deeper plate interface rupture low-permeability materials within the fault, and hence fluids migrate along the megathrust or upwards from the ruptured points (Sibson 1992; Sibson 2013; Gosselin et al. 2020).

The pore pressure within the source regions gradually increases by steady fluid supply and tectonic compression (Saffer and Bekins 1998) ((A) in Figs. 5b and c), whereas it increases suddenly after a transient fluid influx. If fluids are concentrated beneath low-permeability materials, the trapped fluids may

transiently migrate upwards due to the rupturing of the constitutive materials by seismic activities that occur within the oceanic crust and uppermost mantle in this region (Nakano et al. 2013; Mochizuki et al. 2010).

When fluids are transiently supplied to the source region with relatively low pore pressure (but still high compared to the ambient condition), some of the fluids are trapped and increases the pore pressure ((B) in Fig. 5b), while the rest are expelled into the seawater from the margin of the source region (Fig. 5b). The pore pressure at the source region is further steadily and transiently increased by tectonic compaction and continuing fluid supply ((C) in Fig. 5b) and multiple fluid influx (Fig. 4). The resulting high pore pressure at a critical level activates slow earthquakes and decreases during permeability enhancement following slips (Sibson 1992; Sibson 2013; Gosselin et al. 2020) ((D) in Fig. 5b). The amplitude and propagation velocity of ACR waves are sensitive to the seismic structure of the entire accretionary prism. Because the CC drops were recovered prior to slow earthquakes, however, the CC drops responded to temporal variations in the heterogeneous seismic structure at the shallow depths due to the upward fluid migration.

The concurrent CC reductions are possibly caused by two mechanisms; fluid migration activates slow earthquakes by increasing pore pressure at a source region, and slow earthquakes induce upward fluid migration with the breakout of boundaries to trap fluids. Event 9 (Fig. 3d) may correspond to the latter case, because of some delay of the CC reductions relative to the onset of slow earthquakes. Nevertheless, the preceding fluid migration was observed multiple times in the low pore-pressure region, and a slightly preceding event was also observed (Fig. S6a). We therefore consider that the former case probably occurs frequently. When fluids reach the source region with originally high pore pressure in this case, they immediately induce slow earthquakes along with fluid migration from the source region (from (B) to (D) in Fig. 5c). Significantly low shear wave velocities (Vs), indicative of high pore pressure, were indeed estimated within the prism in the western region, compared to Vs in the eastern and central regions (Tonegawa et al. 2017). Our results indicate that pore pressure levels are temporally changed at a fixed position in the eastern and central regions, and high pore pressure exists in the western region (i.e. red and black arrows in Fig. 4 can be interpreted as high and low pore pressure conditions, respectively).

5.3 Other CC reductions

Our results for DONET1 show that preceding and concurrent CC reductions to slow earthquakes tend to occur near the margin of (Events 1–3, 11–13, 16, and 18) and above the source regions of shallow slow earthquakes (Events 4 and 15), respectively (Fig. 4). Moreover, in DONET2, the preceding CC reductions occurred in the central region (node MRE) (Fig. S5e, and Event 19), whereas the concurrent CC reductions occurred in the western region (node MRG) (Fig. 3d, Events 7, 8, and 9). The CC reduction in Event 20 in node MRF may be regarded as an extension of that around node MRE because it can be seen in all

of the station pairs. The occurrence of preceding CC reductions in the western region must be monitored.

For Events 5 and 6, the spatial patterns of the SCCs are completely different. Event 5 prior to the SSE and Event 6 during the SSE may correspond to the margin and inside the source region of the SSE, respectively. Only the SSE of April–May 2018 was followed by the CC reductions in Event 17. While the first CC reduction (Event 17-1 in Fig. S9f) occurred at the margin of the source region, the second (Event 17-2 in Fig. S9g) moved to the source region. The SCC for Event 18 may have occurred inside the source region; however the main location is at the downdip side. For Event 22, sVLFE activities could not been observed in the central region. Although the CC reductions may be related to the sVLFE in the western region, the relation to slow earthquakes for this event remains elusive. A small sVLFE activity, which cannot be observed at land stations, might have occurred in this region.

Long-term CC changes observed in 2017 are also indicative of slow earthquakes (Fig. 3c). Shallow SSEs have recently been detected via seafloor geodetic observations (Yokota and Ishikawa 2020), although its temporal resolution remains low. We found gradual CC reductions during 2017–2018 in the southern parts of DONET1 (Fig. 3c and Fig. S4b) with a negative peak of Event 15 (Fig. S4b). Although the geodetic observation possibly detected an SSE corresponding to Event 15, if it detected a long-term SSE that have not been detected by the borehole pore pressure measurement due to, e.g., the difference of observation locations, the long-term CC reduction corresponds to continuous fluid supply during the long-term SSE. Indeed, the geodetic observation was conducted near the epicentre of the earthquakes shown by the red star in Fig 1 (Yokota and Ishikawa 2020), which is slightly at the down-dip side of the boreholes.

We observed large CC reductions in 2018 at MRD17 (Fig. S5d). Although the reasons for these reductions remain unclear, because the waveform shapes of the stacked CCFs were not significantly varied during 2018, the seismic velocity structure beneath this station might have been affected by copious fluids at a local scale. However, we do not link this event with fluid migration because the CC reductions were quite large with respect to the other reductions. We also observed large CC reductions in 2020 at nodes MRA and MRB (Figs. S5a and b). The CCFs at the nodes during mid-2020 contain large amplitudes at frequencies of 1–5 Hz, and the reasons for the contamination are unclear (natural or artificial event). Therefore, we do not consider these CC reductions as caused by fluid migration.

5.4 Timing and duration of concurrent CC reductions

Previous studies have reported that seismic velocity, seismic anisotropy, and pore-pressure variations occurred during SSEs (Warren-Smith et al. 2019; Zal et al. 2020). It seems that the durations of such variations correspond to the duration of a single SSE (~1 month). The duration of the concurrent CC reductions observed in this study also has a duration of ~1 month. However,

some of those events coincided with slow earthquakes (Events 4, 15, 6 and 21 in Fig. S6), whereas others occurred at the first or latter half of a single episode of slow earthquake activity (Events 7, 8, and 9 in Fig. 2 and Fig. S6). These events may correspond to the intensities of slow earthquake activities during a single episode.

5 Conclusions

Fluid migration plays an important role in activating slow earthquakes within subduction zones. Although fluid migration in a subduction zone may also be inferred from the spatiotemporal variation of slow and ordinary earthquakes (Nakajima & Uchida 2018), the difference of onset times between the two phenomena has not been identified, particularly for the case where fluid migration occurs in advance to earthquake activities. Real-time monitoring of the seismic heterogeneous structure beneath the seafloor shows that such the difference in their timings are present depending on the pore-pressure conditions at source regions, and suggests that the seismic heterogeneous structure probably changes before the occurrences of slow earthquakes in the shallow subduction zone.

Acknowledgments

We thank Masaru Nakano for providing us sVLFE epicenter data. This work was supported by JSPS KAKENHI Grant Number 16H06472, 19H04632 in Scientific Research on Innovative Areas “Science of Slow Earthquake”, and 21H05202 in Scientific Research on Tranformative Research Areas “Science of Slow-to-Fast earthquakes”.

Data

The seismic data of Dense Oceanfloor Network system for Earthquakes and Tsunamis (DONET) from the National Research Institute for Earth Science and Disaster Resilience can be obtained from https://doi.org/10.17598/NIED.0008. NOAA_OI_SST_V2 data provided by the NOAA/OAR/ESRL PSD, Boulder, Colorado, USA, can be obtained from https://www.esrl.noaa.gov/psd/. Sea level data from Copernicus Climate Data Store is from https://cds.climate.copernicus.eu/cdsapp#!/home. The Kuroshio current data from the Japan Coast Guard is from https://www1.kaiho.mlit.go.jp/jhd-E.html. OSCAR third-degree resolution ocean surface currents are from https://doi.org/10.5067/OSCAR-03D01. Significant wave height data provided by The Nationwide Ocean Wave information network for Ports and HArbourS (NOWPHAS) is from https://www.mlit.go.jp/kowan/nowphas/index_eng.html). The catalog of shallow very low frequency earthquake in Takemura et al. (2021) can be obtained from https://doi.org/10.5281/zenodo.5211090. The dataset in dv/v and CC for each pair of two stations obtained in this study (Fig. 3 and Figs. S4–S6) and the data for creating the figures can be downloaded through a repository (doi:10.5281/zenodo.5637605).

References

Akuhara, T., Tsuji, T., & Tonegawa, T. (2020). Overpressured Underthrust

Sediment in the Nankai Trough Forearc Inferred From Transdimensional Inversion of High-Frequency Teleseismic Waveforms. *Geophysical Research Letters*, *47*(15). https://doi.org/10.1029/2020GL088280

Aoi, S., Asano, Y., Kunugi, T., Kimura, T., Uehira, K., Takahashi, N., et al. (2020). MOWLAS: NIED observation network for earthquake, tsunami and volcano. *Earth, Planets and Space*, *72*(1), 126. https://doi.org/10.1186/s40623-020-01250-x

Araki, E., Saffer, D. M., Kopf, A. J., Wallace, L. M., Kimura, T., Machida, Y., et al. (2017). Recurring and triggered slow-slip events near the trench at the Nankai Trough subduction megathrust. *Science*, *356*(6343), 1157–1160. https://doi.org/10.1126/science.aan3120

Ariyoshi, K., Iinuma, T., Nakano, M., Kimura, T., Araki, E., Machida, Y., et al. (2021). Characteristics of Slow Slip Event in March 2020 Revealed From Borehole and DONET Observatories. *Frontiers in Earth Science*, *8*, 600793. https://doi.org/10.3389/feart.2020.600793

Audet, P., & Bürgmann, R. (2014). Possible control of subduction zone slow-earthquake periodicity by silica enrichment. *Nature*, *510*(7505), 389–392. https://doi.org/10.1038/nature13391

Baba, T., Tanioka, Y., Cummins, P. R., & Uhira, K. (2002). The slip distribution of the 1946 Nankai earthquake estimated from tsunami inversion using a new plate model. *Physics of the Earth and Planetary Interiors*, *132*(1–3), 59–73. https://doi.org/10.1016/S0031-9201(02)00044-4

Baba, S., Takemura, S., Obara, K., & Noda, A. (2020). Slow Earthquakes Illuminating Interplate Coupling Heterogeneities in Subduction Zones. *Geophysical Research Letters*, *47*(14). https://doi.org/10.1029/2020GL088089

Brenguier, F., Shapiro, N. M., Campillo, M., Nercessian, A., & Ferrazzini, V. (2007). 3-D surface wave tomography of the Piton de la Fournaise volcano using seismic noise correlations. *Geophysical Research Letters*, *34*(2), 1351–5. https://doi.org/10.1029/2006GL028586

Chevrot, S. (2002). Optimal measurement of relative and absolute delay times by simulated annealing. *Geophysical Journal International*, *151*(1), 164–171. https://doi.org/10.1046/j.1365-246X.2002.01755.x

ESR. (2009). *OSCAR third degree resolution ocean surface currents. Ver. 1* (p. 4). PO.DAAC, CA, USA. https://doi.org/10.5067/OSCAR-03D01

Gosselin, J. M., Audet, P., Esteve, C., McLellan, M., Mosher, S. G., & Schaeffer, A. J. (2020). Seismic evidence for megathrust fault-valve behavior during episodic tremor and slip. *Science Advances*, *6*, eaay5174.

Hirose, F., Nakajima, J., & Hasegawa, A. (2008). Three-dimensional seismic velocity structure and configuration of the Philippine Sea slab in southwestern Japan estimated by double-difference tomography. *Journal of Geophysical*

Research, *113*(B9), B09315. https://doi.org/10.1029/2007JB005274

Hirose, T., Nakahara, H., & Nishimura, T. (2019). A Passive Estimation Method of Scattering and Intrinsic Absorption Parameters From Envelopes of Seismic Ambient Noise Cross-Correlation Functions. *Geophysical Research Letters*, *46*(7), 3634–3642. https://doi.org/10.1029/2018GL080553

Hirose, T., Nakahara, H., Nishimura, T., & Campillo, M. (2020). Locating Spatial Changes of Seismic Scattering Property by Sparse Modeling of Seismic Ambient Noise Cross-Correlation Functions: Application to the 2008 Iwate-Miyagi Nairiku (*Mw*6.9), Japan, Earthquake. *Journal of Geophysical Research: Solid Earth*, *125*(6). https://doi.org/10.1029/2019JB019307

Ikeda, H., & Takagi, R. (2019). Coseismic changes in subsurface structure associated with the 2018 Hokkaido Eastern Iburi Earthquake detected using autocorrelation analysis of ambient seismic noise. *Earth, Planets and Space*, *71*, 72. https://doi.org/10.1186/s40623-019-1051-5

Ikeda, T., & Tsuji, T. (2018). Temporal change in seismic velocity associated with an offshore MW 5.9 Off-Mie earthquake in the Nankai subduction zone from ambient noise cross-correlation. *Progress in Earth and Planetary Science*, *5*, 62. https://doi.org/10.1186/s40645-018-0211-8

Kameda, J., Yamaguchi, A., Saito, S., Sakuma, H., Kawamura, K., & Kimura, G. (2011). A new source of water in seismogenic subduction zones. *Geophysical Research Letters*, *38*(22), n/a-n/a. https://doi.org/10.1029/2011GL048883

Kaneda, Y., Kawaguchi, K., Araki, E., Matsumoto, H., Nakamura, T., Kamiya, S., et al. (2015). Development and application of an advanced ocean floor network system for megathrust earthquakes and tsunamis. In P. Favali, L. Beranzoli, & A. De Santis (Eds.), *SEAFLOOR OBSERVATORIES* (Vols. 1–Chapter 25, pp. 643–662). Berlin, Heidelberg: Springer Berlin Heidelberg. https://doi.org/10.1007/978-3-642-11374-1_25

Katayama, I., Terada, T., Okazaki, K., & Tanikawa, W. (2012). Episodic tremor and slow slip potentially linked to permeability contrasts at the Moho. *Nature Geoscience*, *5*, 731–734. https://doi.org/10.1038/ngeo1559

Kawaguchi, K., Kaneko, S., Nishida, T., & Komine, T. (2015). Construction of the DONET real-time seafloor observatory for earthquakes and tsunami monitoring. In P. Favali, L. Beranzoli, & A. De Santis (Eds.), *SEAFLOOR OBSERVATORIES* (Vols. 1–Chapter 10, pp. 211–228). Berlin, Heidelberg: Springer Berlin Heidelberg. https://doi.org/10.1007/978-3-642-11374-1_10

Kitajima, H., & Saffer, D. M. (2012). Elevated pore pressure and anomalously low stress in regions of low frequency earthquakes along the Nankai Trough subduction megathrust. *Geophysical Research Letters*, *39*(23), L23301. https://doi.org/10.1029/2012GL053793

Kodaira, S. (2004). High Pore Fluid Pressure May Cause Silent Slip in the Nankai Trough. *Science*, *304*(5675), 1295–1298. https://doi.org/10.1126/scie

nce.1096535

Maeda, T., Takemura, S., & Furumura, T. (2017). OpenSWPC: an open-source integrated parallel simulation code for modeling seismic wave propagation in 3D heterogeneous viscoelastic media. *Earth, Planets and Space*, *69*(1), 102. https://doi.org/10.1186/s40623-017-0687-2

Mochizuki, K., Nakahigashi, K., Kuwano, A., Yamada, T., Shinohara, M., Sakai, S., et al. (2010). Seismic characteristics around the fault segment boundary of historical great earthquakes along the Nankai Trough revealed by repeated long-term OBS observations. *Geophysical Research Letters*, *37*(9), n/a-n/a. https://doi.org/10.1029/2010GL042935

Nakajima, J., & Hasegawa, A. (2016). Tremor activity inhibited by well-drained conditions above a megathrust. *Nature Communications*, *7*, 13863. https://doi.org/10.1038/ncomms13863

Nakajima, J., & Uchida, N. (2018). Repeated drainage from megathrusts during episodic slow slip. *Nature Geoscience*, *11*(5), 351–356. https://doi.org/10.1038/s41561-018-0090-z

Nakano, M., Nakamura, T., Kamiya, S., Ohori, M., & Kaneda, Y. (2013). Intensive seismic activity around the Nankai trough revealed by DONET ocean-floor seismic observations. *Earth, Planets and Space*, *65*(1), 5–15. https://doi.org/10.5047/eps.2012.05.013

Nakano, M., Hori, T., Araki, E., Takahashi, N., & Kodaira, S. (2016). Ocean Floor Networks Capture Low-Frequency Earthquake Event. *EOS*, *97*. https://doi.org/10.1029/2016EO052877

Nakano, M., Hori, T., Araki, E., Kodaira, S., & Ide, S. (2018). Shallow very-low-frequency earthquakes accompany slow slip events in the Nankai subduction zone. *Nature Communications*, *9*, 984. https://doi.org/10.1038/s41467-018-03431-5

Obara, K., & Kato, A. (2016). Connecting slow earthquakes to huge earthquakes. *Science*, *353*(6296), 253–257. https://doi.org/10.1126/science.aaf1512

Obermann, A., Planès, T., Larose, E., & Campillo, M. (2013). Imaging preeruptive and coeruptive structural and mechanical changes of a volcano with ambient seismic noise. *Journal of Geophysical Research: Solid Earth*, *118*(12), 6285–6294. https://doi.org/10.1002/2013JB010399

Park, J.-O., Fujie, G., Wijerathne, L., Hori, T., Kodaira, S., Fukao, Y., et al. (2010). A low-velocity zone with weak reflectivity along the Nankai subduction zone. *Geology*, *38*(3), 283–286. https://doi.org/10.1130/G30205.1

Rost, S., & Thomas, C. (2002). Array seismology: Methods and applications. *Reviews of Geophysics*, *40*(3), 2-1-2–27. https://doi.org/10.1029/2000RG000100

Saffer, D. M., & Bekins, B. A. (1998). Episodic fluid flow in the Nankai accretionary complex: Timescale, geochemistry, flow rates, and fluid budget, *103*(B12), 30351–30370.

Saffer, D. M., Underwood, M. B., & McKiernan, A. W. (2008). Evaluation of factors controlling smectite transformation and fluid production in subduction zones: Application to the Nankai Trough. *Island Arc*, *17*(2), 208–230. https://doi.org/10.1111/j.1440-1738.2008.00614.x

Saffer, D. M., & Tobin, H. J. (2011). Hydrogeology and Mechanics of Subduction Zone Forearcs: Fluid Flow and Pore Pressure. *Annual Review of Earth and Planetary Sciences*, *39*(1), 157–186. https://doi.org/10.1146/annurev-earth-040610-133408

Sánchez-Pastor, P., Obermann, A., & Schimmel, M. (2018). Detecting and Locating Precursory Signals During the 2011 El Hierro, Canary Islands, Submarine Eruption. *Geophysical Research Letters*, *45*(19), 10,288-10,297. https://doi.org/10.1029/2018GL079550

Sen, M. K. & Stoffa, P. L. (1995). *Global Optimization Methods in Geophysical Inversion*. 1–294 (Elsevier Science Ltd.). doi:10.1017/CBO9780511997570

Sens-Schonfelder, C., & Wegler, U. (2006). Passive image interferometry and seasonal variations of seismic velocities at Merapi Volcano, Indonesia. *Geophysical Research Letters*, *33*(21), 547–5. https://doi.org/10.1029/2006GL027797

Shapiro, N. M., Campillo, M., Stehly, L., & Ritzwoller, M. H. (2005). High-Resolution Surface-Wave Tomography from Ambient Seismic Noise. *Science*, *307*(5715), 1615–1618. https://doi.org/10.1126/science.1108339

Shelly, D. R., Beroza, G. C., & Ide, S. (2007). Non-volcanic tremor and low-frequency earthquake swarms. *Nature*, *446*(7133), 305–307. https://doi.org/10.1038/nature05666

Sibson, R. H. (1992). Implications of fault-valve behaviour for rupture nucleation and recurrence. *Tectonophysics*, *211*(1–4), 283–293. https://doi.org/10.1016/0040-1951(92)90065-E

Sibson, R. H. (2013). Stress switching in subduction forearcs: Implications for overpressure containment and strength cycling on megathrusts. *Tectonophysics*, *600*, 142–152. https://doi.org/10.1016/j.tecto.2013.02.035

Takemura, S., Matsuzawa, T., Noda, A., Tonegawa, T., Asano, Y., Kimura, T., & Shiomi, K. (2019). Structural Characteristics of the Nankai Trough Shallow Plate Boundary Inferred From Shallow Very Low Frequency Earthquakes. *Geophysical Research Letters*, *46*(8), 4192–4201. https://doi.org/10.1029/2019GL082448

Takemura, S., Yabe, S., & Emoto, K. (2020). Modelling high-frequency seismograms at ocean bottom seismometers: effects of heterogeneous structures on source parameter estimation for small offshore earthquakes and shallow

low-frequency tremors. *Geophysical Journal International*, *223*(3), 1708–1723. https://doi.org/10.1093/gji/ggaa404

Takemura, S., Obara, K., Shiomi, K., & Baba, S. (2021). Spatiotemporal variations of shallow very low frequency earthquake activity southeast off the Kii Peninsula, along the Nankai Trough, Japan (preprint). https://doi.org/10.1002/essoar.10507824.1

Tonegawa, T., Fukao, Y., Takahashi, T., Obana, K., Kodaira, S., & Kaneda, Y. (2015). Ambient seafloor noise excited by earthquakes in the Nankai subduction zone. *Nature Communications*, *6*(1), 6132. https://doi.org/10.1038/ncomms7132

Tonegawa, T., Araki, E., Kimura, T., Nakamura, T., Nakano, M., & Suzuki, K. (2017). Sporadic low-velocity volumes spatially correlate with shallow very low frequency earthquake clusters. *Nature Communications*, *8*, 2048. https://doi.org/10.1038/s41467-017-02276-8

Tonegawa, T., Kimura, T., & Araki, E. (2021). Near-Field Body-Wave Extraction From Ambient Seafloor Noise in the Nankai Subduction Zone. *Frontiers in Earth Science*, *8*, 610993. https://doi.org/10.3389/feart.2020.610993

Tsuji, T., Kamei, R., & Pratt, R. G. (2014). Pore pressure distribution of a mega-splay fault system in the Nankai Trough subduction zone: Insight into up-dip extent of the seismogenic zone. *Earth and Planetary Science Letters*, *396*(C), 165–178. https://doi.org/10.1016/j.epsl.2014.04.011

Warren-Smith, E., Fry, B., Wallace, L., Chon, E., Henrys, S., Sheehan, A., et al. (2019). Episodic stress and fluid pressure cycling in subducting oceanic crust during slow slip. *Nature Geoscience*, *12*, 475–481. https://doi.org/10.1038/s41561-019-0367-x

Wiener, N. (1949). *Extrapolation, Interpolation, and Smoothing of Stationary Time Series*. (MIT/John Wiley).

Yokota, Y., & Ishikawa, T. (2020). Shallow slow slip events along the Nankai Trough detected by GNSS-A. *Science Advances*, *6*, eaay5786.

Zal, H. J., Jacobs, K., Savage, M. K., Yarce, J., Mroczek, S., Graham, K., et al. (2020). Temporal and spatial variations in seismic anisotropy and V/V ratios in a region of slow slip. *Earth and Planetary Science Letters*, *532*, 115970. https://doi.org/10.1016/j.epsl.2019.115970

Figure 1. Map showing locations of stations and seismic velocity changes (*dv/v)*. Yellow triangles and magenta circles represent DONET stations and shallow very low frequency earthquakes (sVLFE) during August 2015–April 2016 (Nakano et al. 2016; 2018). The red star shows the location of the earthquake that occurred southeast of the Kii Peninsula on 1 April 2016. Grey triangles indicate the locations of the boreholes used in Araki et al. (2019) and Ariyoshi et al. (2021). Nodes KMC and MRG (pink) are used in Fig. 3. Orange lines

represent the depth contour of the Philippine Sea Plate (Baba et al. 2002; Hirose et al. 2008).

Figure 2. Example of the processing of stretching. (a) CCFs for the KMD14–KMD15 station pair over the observation period at 0.5–2.0 Hz. (b) Delay times of CCFs in (a) with respect to the reference CCF stacked over the first 1 year. The arrow indicates the timing of the off-Mie earthquake. (c) Parts of (black line) the CCF (203 Julian day in 2013) and (red line) reference CCF at a lag time of 14–18 s. (d) (black line) Cross-correlation function and (red line) Wiener filter between the two CCFs shown in (c).

Figure 3. Temporal changes of seismic velocity and heterogeneity. (a) The resulting dv/v for 6 pairs of 4 stations of node KMC with (orange) 1 uncertainties for $\pm$50 days. Pink, light-brown, and gray regions represent the periods of SSEs from Araki et al. (2017) and Ariyoshi et al. (2021), a large slow earthquake activity, and data gaps. Red star shows the earthquake in Fig. 1. (b) Same as (a), but for node MRG. Light-blue regions indicate the periods of sVLFE activities (Nakano et al. 2016; 2018; Takemura et al. 2019; Baba et al. 2020). (c) Temporal CC variation for node KMC. Black and gray arrows indicate the preceding CC reductions observed around node KMC and other regions in the southern part of DONET, respectively. Red arrow shows concurrent CC reductions. Other numbers are provided in Fig. 4. An SSE was detected by the seafloor geodetic observation in 2017 (Yokota and Ishikawa 2020). (d) Same as (c), but for node MRG. Blue arrow represents concurrent CC reductions with a slight delay.

Figure 4. Identification of CC reductions. (a) CC variations for station pairs in the southern part of DONET1 (nodes KMB, KMC, and KMD), which are aligned by the central locations of station pairs from south (bottom) to north (top). Black and red arrows indicate pairs that show preceding and concurrent CC variations to slow earthquakes, respectively. Blue arrow corresponds to concurrent CC reductions but with a delay (Event 9). Light-blue arrow corresponds to CC variations associated with large earthquakes (Event 1 of the 2011 Tohoku-Oki earthquake, and Event 14 of the earthquake shown in Fig. 1). More details for each event are described in the text and Table S1. Pink (Araki et al. 2017; Ariyoshi et al. 2021) and light-brown regions are the periods of slow earthquakes. Periods from first CC drop and subsequent slow earthquake activities are noted. (b) Same as (a), but for the southern part of DONET2 (MRE, MRF, and MRG), which are aligned by the central locations of station pairs from west (bottom) to east (top). Dark-blue and light-blue represent sVLFE activities around MRE (central region) and MRF–MRG (western region), respectively (Nakano et al. 2016; 2018; Takemura et al. 2019; Baba et al. 2020). (c) Same as (a), but the CC reductions that are larger than twice the standard deviation are only plotted. (d) Same as (c), but for DONET2.

Figure 5. Spatiotemporal relationship between fluid supply, slow earthquakes, and pore pressure. (a) Velocity increase at shallow depths due to fluid drainage to seawater, with a geological interpretation of Akuhara et al. (2020). Blue

shades represent the amount of fluid. (b) Slow earthquake generation and fluid supply in the source region for low pore pressure. Beach balls and orange lines show sVLFEs and SSEs. Magenta arrows indicate fluid flow. (Right) Temporal variation in pore pressure (P_f) at the source region for low pore pressure. Pink and light-orange areas indicate the amount of fluid supply to the source region and the activity period of slow earthquakes, respectively. The characters of A–D represent stages of P_f variations (see details in the text). (c–d) Same as (b), but for high pore pressure.

Figure 6. Spatiotemporal variations of scattering coefficient changes (Δg). (a) Map showing the scattering coefficient changes in the southern part of DONET1 for Event 1 (the event numbers are shown in Fig. 4). Dashed blue-boxes represent the regions of SSEs detected by Araki et al. (2017) (the slip region only in the dip direction was referred from the paper). Light-blue triangles show the locations of the DONET stations for nodes KMB, KMC and KMD. (b–f) Same as (a), but for Events 2–6. Purple and light-brown circles in (c) and (f) show sVLFE locations during 2015 (Nakano et al. 2016; 2018) and December 2020–January 2021 (Takemura et al. 2021)